Implementation of subsurface transport processes in the low-dimensional integrated hydrological model NIHM

Mouna Chaguer, Sylvain Weill, Philippe Ackerer, Frederick Delay

Implementation of subsurface transport processes in the low-dimensional integrated hydrological model NIHM

Mouna Chaguer[1], Sylvain Weill[1 *], Philippe Ackerer[1], Frederick Delay[1]

[1] Institut Terre et Environnement de Strasbourg, UMR 7063 CNRS, Université de Strasbourg, Engees, 5 Rue René Descartes, 67000 Strasbourg, France.

[*] Corresponding author: sylvain.weill@engees.unistra.fr

Abstract

Solute transport models based on the resolution of the 3-D Advection-Dispersion (AD) equation are frequently plagued by several numerical problems, which add to the high computational cost. The hydrological model NIHM (Normally Integrated Hydrological Model) was recently proposed as a tool simulating the hydrological responses of watersheds with shallow saturated aquifers by coupling surface flow and a low-dimensional subsurface system, including the vadose zone. In this paper, we couple the low-dimensional flow model NIHM with a transport module solving the AD to propose an approach that enables to reduce the dimensionality of both the flow and transport problems. In NIHM, the low-dimensionality in the subsurface compartment results from an integration along the local direction normal to the bedrock of the aquifer. NIHM was previously evaluated and applied to actual hydrosystems—without addressing mass transfers—and it showed its ability to capture various hydrological responses even from complex systems. However, the relevance of a low-dimensional approach to transport is not proven yet as the model reduction could also render approximated velocity fields inappropriate to mass transfer problems. The accuracy and computational efficiency of the proposed model have been thoroughly examined through various synthetic test cases under different hydrodynamic conditions to assess the influence of

the reduction of dimensionality on solute transport simulations. The findings of this study demonstrate that the reduction of dimension remains suited to predicting solute transport behaviors in shallow subsurface systems while providing an important gain in computation time. This might be promising for various applications dealing with groundwater quality.

Keywords: subsurface solute transport, model reduction, low-dimensional model, advection-dispersion equation, transport scheme

1- Introduction

Water resources are polluted and contaminated by different anthropogenic activities. Major sources of pollutants may include intensive farming practices, the pharmaceutical manufacturing industry, urbanization, population growth, and improper sewer systems (Burri et al., 2019). Contaminants transported in the groundwater may remain for decades, resulting in long-term water quality degradation and many other environmental issues. Contaminant residence times usually depend on the properties and characteristics of the aquifer, the overall hydrological conditions, and the physical-chemical characteristics of the contaminant itself. By ranging from weeks to several years, these residence times are able to threaten groundwater renewability and usability (Chapman and Parker, 2005; Moeck et al., 2017). Exposure to water pollution can generate severe problems and might become a serious concern to human health and the environment (Wakida and Lerner, 2005). Tackling these environmental challenges has shed light on the importance of effective groundwater

management tools for water quality assessment and prediction.

Mathematical modeling of solute transport in different hydrological systems has received particular attention from the hydrological community for years. A tremendous number of studies have been specifically designed either in the theoretical or the applied domains with regard to groundwater contamination (Carnahan et al., 1969; Leij et al., 1991; Selim, 1992; Wu and Jeng, 2017). Several analytical approximations and numerical approaches have been developed to reproduce solute transport behaviors in porous media (Barry and Parker, 1987; Bosma and Van der Zee, 1992; Leij and Van Genuchten, 1995; Dou et al., 1997; Shan and Javandel, 1997). The migration of contaminant species associated with groundwater flow usually obeys elementary mechanisms such as advection, diffusion-dispersion, and reaction. In many groundwater transport models, mass transport through porous media is described by the Advection-Dispersion (AD) equation (Bear, 1972; Barry, 1992). This equation can be solved either by numerical or analytical methods. Analytical solutions to the AD are available for specific initial and boundary conditions, which mostly results in an applicability limited to simple geometries and homogeneous aquifers (Konikow et al., 1997; Tartakovsky, 2000; Rocha et al., 2007). Due to the complexity of actual natural systems, numerical methods for solving the AD have been developed and are considered today as the best tools to account for the effect of aquifer heterogeneities, various boundary conditions, and diverse transient source-sink terms in groundwater solute transport processes (e.g., Craig and Rabideau, 2006; Boso et al., 2013). For instance, the modular 3-D transport model MT3DMS (Zheng and Wang, 1999) was used for several applications to simulate changes over time and space in concentrations of groundwater contaminants (Zheng et al., 2012; Colombo et al., 2019; Lyra et al., 2021).

Physically-based models solving the AD with a full 3-D approach often face crucial problems, mainly associated with numerical approximations of the continuous AD (e.g.,

numerical dispersion of many discrete schemes), the complexity of the discretization process, and the high demand in computational resources, etc. Fully physically-based models such as HydroGeoSphere (Therrien and Sudicky 1996; Graf and Therrien, 2005) and MODFLOW (McDonald and Harbaugh, 1988; Harbaugh et al., 2000) are capable of simulating the fate of contaminants in groundwater and have been commonly used for a wide variety of problems in hydrology. However, with the classical computation resources available for a majority of practitioners, but also researchers, these models may need several days for running a single transport scenario when applied to large systems. Therefore, large problems involving complex geometries and complicated systems render numerical solutions prohibitively expensive.

Alternative numerical approaches have drawn the attention of both the hydrological and applied mathematics communities with the aim to reduce this computational burden and describe solute transport processes in a computationally efficient manner (e.g., Robinson et al., 2012; Rizzo et al., 2018). The main idea is to make simpler physically-based models in favor of faster computation and wider ranges of applications for groundwater management problems. One of the interesting outcomes of these investigations is the development of low-dimensional hydrological models for flow, based on the reduction of the dimensionality of the problem (Troch et al., 2003; Pan et al., 2015; Delay and Ackerer, 2016; Kong et al., 2016; Weill et al., 2017). However, only a few contributions assessed the effects of reduced dimensionality in simulating subsurface solute transport; most studies targeted the flow problem in watersheds.

Regarding transport, the majority of recent low-dimensional models mentioned in the literature are based on the POD (proper orthogonal decomposition) method. This approach was introduced by Sirovich in 1987. As a first step, a collection of snapshots is stored by running the original fully-dimensional model. Then, as a second step, the POD technique is

applied with the resulting singular vectors used as a basis for projection onto a subspace of lower dimensionality than the original model (Robinson et al., 2012). Nevertheless, some non-linearities associated with many real-world groundwater systems may affect the correctness of the POD model. Another downside of the technique is the need for prior runs with a complete model, including the imperative representation of the complete system before proceeding with the dimensionality reduction. Stated differently, collecting beforehand an ensemble of reliable model responses for the fully dimensioned system is mandatory.

Other approaches are now available. For example, a low-dimensional approach was recently proposed in the hydrological model NIHM (Normally Integrated Hydrological Model; Pan et al., 2015; Weill et al., 2017; Jeannot et al., 2018, 2019). This model couples a low-dimensional (2-D) subsurface model to a 2-D overland flow and 1-D river flow and was shown to be efficient in reproducing the flow response of various complex hydrological systems (Jeannot et al., 2018, 2019). Unlike simpler 2-D models (mainly aimed at simulating the behavior of the saturated zone under planar horizontal flow, that is, by following the so-called Dupuit assumption), NIHM handles both the vadose and the saturated zones of the subsurface within a single 2-D compartment. Nevertheless, it is worth noting that NIHM was designed to mimic shallow subsurface systems.

The integration of the flow equation along a direction normal to bedrock simplifies the infiltration process from the surface within the vadose zone (for details, see Jeannot et al., 2018, 2019). In short, infiltration is simply viewed as a water transfer from the surface to the subsurface, which changes over time and space, the mean saturated hydraulic head evaluated along the direction of integration. With thick vadose zones, NIHM might render rough local evaluations of mean water fluxes that do not completely depict the local flow processes in the vadose zone compared to a complete 3-D resolution of the Richards equation. That being said, and especially regarding the present study, contamination problems of subsurface water are

126 all the more frequent when the aquifer is shallow. This feature justifies a study on the
127 consequences of the dimensionality reduction for flow onto solute transport.

128 The aim of the present contribution is to assess if the low-dimensional method
129 implemented in NIHM can be extended to efficiently describe subsurface transport. An
130 approach coupling the flow module of NIHM and a 2-D integrated advection-dispersion
131 transport module based is proposed. This results in the so-called NIHM-T low dimensional
132 flow and transport models. The evaluation of the approach is carried out through the
133 comparison of results produced by NIHM-T and those produced by a fully dimensioned
134 version of the code TRACES ((Siegel et al, 1997, Younes et al, 2010). The latter solves via
135 advanced numerical methods a 3-D Richards equation for flow in the vadose and saturated
136 zones, and a 3-D advection-dispersion equation for solute transport. It is worth noting that the
137 model NIHM is only devoted to solving flow in the various compartments of a watershed.
138 The "T" (for transport) module inherits from the experienced strategy and the numerical
139 techniques of TRACES, in its two-dimensional version. The resulting transport module is
140 employed for solving a 2-D integrated AD with velocity fields inherited from the calculations
141 by NIHM for flow. This not only avoids the complete implementation of a transport module
142 in NIHM but also facilitates the comparison between transport scenarios from a 2-D
143 dimensionally reduced model and a full 3-D approach. Eventual discrepancies between both
144 formalisms cannot be associated with eventual numerical differences by solving 2-D versus 3-
145 D transport with different numerical methods. The comparisons discussed hereafter are only
146 the consequences of reducing the dimensionality of flow in a simplified subsurface model.

147 The paper is structured as follows: We first introduce the physical and mathematical
148 models for subsurface flow and solute transport in porous media. Then, the coupling
149 algorithm between the models NIHM and the transport module (inheriting from TRACES in
150 its 2-D version, for the coupling with NIHM - flow) will be outlined. Finally, the effects of

reducing the dimensionality of the flow problem for solute transport will be detailed through applications to different synthetic test cases.

2. Low-dimensional modeling of flow and transport in the subsurface

The following section is dedicated to the description of the low-dimensional flow and transport modeling approaches. The subsurface model NIHM is first briefly presented. The low-dimensional transport equation is then described. The resolution strategy—including a coupling between NIHM and the (2-D) transport module—is detailed before giving the indicators that allow for the comparison of 2-D integrated transport results and those from full 3-D calculations.

2-1- Low-dimensional subsurface flow model NIHM

Subsurface flow modeling is carried out using the low-dimensional subsurface module of the integrated hydrological model NIHM (Pan et al., 2015; Jeannot et al., 2018). The 2-D subsurface equation is derived from the integration of the 3-D Richards equation (Richards, 1931) along a direction normal to the bottom of the aquifer, within a local Eulerian coordinate system (x, y, z) defined by directions (x, y) in the bedrock plane and (z) normal to the bedrock. The integration bounds are the bedrock elevation z_b and the soil surface elevation z_s . After integration along direction *z*, the resulting low-dimensional (2-D) subsurface flow equation comes down to (e.g., Jeannot et al., 2018):

$$\int_{z_b}^{z_s}\left(\frac{\partial \theta}{\partial t}+Ss\,S_w(\theta)\frac{\partial h}{\partial t}\right)dz+\int_{z_b}^{z_s}\nabla.\left(-\mathbf{K}(\theta)\nabla h\right)dz=\int_{z_b}^{z_s}q_w dz \quad (1)$$

where θ [-] is the water content, S_w [–] is the water saturation, Ss [L^{-1}] is the specific storage capacity of the medium, $\mathbf{K}$ [LT^{-1}] is the tensor of hydraulic conductivity, h [L] is the hydraulic head, and q_w [T^{-1}] is a source-sink term. The unsaturated soil hydraulic functions describing the nonlinear relationships between saturation, water content, and hydraulic conductivity are modeled using the Mualem and Van Genuchten equations (Van Genuchten, 1980).

This low-dimensional approach assumes that the distribution of water pressure throughout the soil profile (from the bedrock to the soil surface) is simplified to evaluate the integral terms in Eq. (1) by calculating a single head value at each location (x, y) and thus resulting in a 2-D approach. For the sake of simplicity, it is assumed that the pressure distribution along the direction normal to the bedrock is hydrostatic, that is, the flow is mainly parallel to bedrock.

As a consequence, the description of flow through the unsaturated zone is simplified. Rainfall is directly applied as a recharge flux making the water table rise. Moisture in the unsaturated zone increases accordingly by following the hydrostatic (capillary) pressure hypothesis and the relationships between pressure and water saturation. Infiltration fronts and moisture storage in the unsaturated zone are not described the same way as would render a Richards-based approach. Furthermore, the time variation of the water content θ is null in the saturated zone (with S_w=1), and the term in Eq. (1), including the specific storage capacity Ss, is usually negligible compared to the time variation of the water content within the unsaturated profile.

Introducing the water table elevation z_w as an integral bound and using the two previous assumptions, Eq. (1) is rewritten as:

198 $$\frac{\partial \bar{\theta}}{\partial t} + \bar{S}\frac{\partial h}{\partial t} + \nabla.\left(-\bar{\mathbf{T}}\nabla h\right) = Q_w$$

199 (2)

200 where $\bar{\theta} = \int_{z_w}^{z_z} \theta(z)\,dz$, $\bar{S} = Ss_{sat}h$, and $\bar{\mathbf{T}} = \mathbf{K}_{sat}h + \int_{z_w}^{z_s} \mathbf{K}_{xy}\left(\theta(z)\right)dz$.

201 Note that in Eq. (2), h has become a mean hydraulic head along the direction normal to
202 bedrock. $\mathbf{K}_{sat}$ and Ss_{sat} are the depth-averaged saturated hydraulic conductivity tensor and
203 specific storage capacity in the saturated zone, respectively. Eq. (2) is solved over an irregular
204 triangular mesh using a Crouzeix-Raviart finite element (CRFE) scheme (Crouzeix and
205 Raviart, 1973), an implicit scheme in time, and a Newton-Raphson algorithm to handle
206 nonlinearity. This approach has been tested in various hydrological configurations and
207 successfully applied to several real-world systems (Pan et al., 2015; Weill et al., 2017,
208 Jeannot et al., 2018). The results show that reducing dimensionality for flow preserves the
209 main characteristics of the flow dynamics in a watershed while reducing the computation
210 burden significantly.

211

212 ***2-2- Governing equation for low-dimensional subsurface transport***

213 The low-dimensional subsurface solute transport equation is derived using the same
214 reduction approach as the one presented previously for subsurface flow in NIHM but applied
215 to the classical advection-dispersion equation. This equation is widely used to describe
216 transport of solute and can be written as:

217 $$\frac{\partial(\theta C)}{\partial t} = \nabla.\left(\theta \mathbf{D}\nabla C - \mathbf{q}C\right) + q_s$$

218 (3)

219 where C [ML^{-3}] is the solute concentration, $\mathbf{D}$ [L^2T^{-1}] is the dispersion/diffusion tensor
220 (including hydrodynamic dispersion and molecular diffusion), $\mathbf{q}$[LT^{-1}] is the Darcy velocity

of water, θ [-] is the water content, and q_s [$ML^{-3}T^{-1}$] is the source-sink term. The dispersion/diffusion tensor is defined by (Zheng and Bennett, 2002):

$$\mathbf{D} = D_{pm}\mathbf{I} + \mathbf{D}_H \tag{4}$$

$$D_{H,i,j} = \alpha_T \|\mathbf{u}\| \delta_{ij} + \frac{(\alpha_L - \alpha_T) u_i u_j}{\|\mathbf{u}\|} \tag{5}$$

$$D_{pm} = D_m . \tau \tag{6}$$

where α_L [L] is the longitudinal dispersivity, α_T [L] is the horizontal or vertical transverse dispersivity assumed identical, $\mathbf{u}$ [LT^{-1}] is the mean pore velocity vector, $(\mathbf{u} = \mathbf{q}/\theta)$, $\mathbf{D}$ [L^2T^{-1}] is the dispersion tensor, $\mathbf{I}$ [-] is the identity matrix, D_{pm} [L^2T^{-1}] is the molecular diffusion coefficient in the porous material, D_m[L^2T^{-1}] is the molecular diffusion coefficient in pure water, and τ [-] is the tortuosity factor.

In our approach, Eq. (3) is integrated along a direction normal to the bottom of the aquifer within the same local Eulerian coordinate system (x, y, z) as defined for the low-dimensional 2-D subsurface flow model. The integration bounds are the bedrock elevation z_b and the soil surface elevation z_s. Eq. (3) becomes:

$$\int_{z_b}^{z_s} \frac{\partial(\theta C)}{\partial t} dz = \int_{z_b}^{z_s} \nabla.(\theta \mathbf{D} \nabla C) dz + \int_{z_b}^{z_s} \nabla.(-\mathbf{q} C) dz + \int_{z_b}^{z_s} q_s dz \tag{7}$$

Applying the Leibnitz rule to each integral in Eq. (7) would transform, for example, $\int_a^b \partial f / \partial t \, dz$ into $\frac{\partial}{\partial t}\int_a^b f \, dz - f(b)\partial b/\partial t + f(a)\partial a/\partial t$, with the same transform also valid for the divergent operator ∇. With integration bounds z_b and z_s considered as constant over time and with negligible (local) gradient over space, Eq. (7) can be rewritten as:

240 $$\frac{\partial}{\partial t}\int_{z_b}^{z_s}(\theta C)dz = \nabla.\int_{z_b}^{z_s}(\theta \mathbf{D}\nabla C)dz + \nabla.\int_{z_b}^{z_s}(-\mathbf{q}C)dz + Q_s \quad (8)$$

241 Q_s being the local integral over *z* of the source-sink term q_s.

242 The low-dimensional model assumes a hydrostatic head distribution in a direction
243 normal to the bedrock, that is, a velocity parallel to the bedrock. With no flow components
244 along the local direction *z*, the solute transport also becomes two-dimensional, handling mean
245 concentration and transport parameters $(\mathbf{q},\mathbf{D},...)$ uniform over *z*. By keeping the notation *C*
246 as the mean concentration over *z*, and extracting it from the integrals over *z* (as it does not
247 depend on *z*), Eq. (8) becomes:

248 $$\frac{\partial}{\partial t}\left(C\int_{z_b}^{z_s}\theta(z)dz\right) = \nabla_{x,y}.\left(\nabla_{x,y}C\int_{z_b}^{z_s}\theta\mathbf{D}(z)dz\right) - \nabla_{x,y}.\left(C\int_{z_b}^{z_s}\mathbf{q}(z)dz\right) + Q_s \quad (9)$$

249 with $\nabla_{x,y}$ the divergent or the gradient operators limited to the directions (x,y). Simplifying
250 the notation in Eq. (9) renders:

251 $$\frac{\partial(\overline{\theta}C)}{\partial t} = \nabla_{x,y}.\left(\overline{\theta\mathbf{D}}.\nabla_{x,y}C - \overline{\mathbf{q}}C\right) + Q_s \quad (10)$$

252 with (2-D) mean parameters: $\overline{\theta} = \int_{z_b}^{z_s}\theta(z)\,dz$, $\overline{\mathbf{q}} = \int_{z_b}^{z_s}\mathbf{q}(z)\,dz$, $\overline{\theta\mathbf{D}} = \int_{z_b}^{z_s}\theta\mathbf{D}(z)\,dz$

253 ***2-3- Solution strategy***

254 The implementation of the low-dimensional transport approach is based on the
255 coupling of NIHM (flow) with a solute transport module ("T" module) inheriting from the 2-
256 D numerical implementations in TRACES. NIHM is used to solve flow in two dimensions
257 over the whole simulated period. The resulting water content and velocity fields required to
258 solve the transport equation in Eq. (10) are stored at different time steps. These flow data are
259 then used as input by the 2-D version of the transport module "T" at the corresponding time.

260 To avoid mapping the data from a flow mesh to the transport mesh, both numerical
261 implementations share the same triangular mesh.

262 By default, the NIHM solutions for flow are saved at each of the time steps. These
263 time steps might be very small due to the non-linearity of the flow equation. To reduce the
264 storage requirements and computer time necessary to solve the transport problem, the results
265 from NIHM can be saved at selected time steps. The selection criterion used here to save the
266 flow data or not is based on the local (i.e., at the element level) variation of the velocity
267 between time steps. If the velocity difference between two successive time steps is greater
268 than 1% in one element of the mesh, the flow data (water content and velocity fields) are
269 saved. If not, flow data are averaged over *n-1* successive time steps until the difference in
270 local velocities (at the element scale) between the times t_1 and t_n is greater than 1% in at least
271 one element of the mesh.

272 In the transport model, the resolution of the AD equation – both in 2-D and 3-D
273 configurations – is performed using an operator splitting approach. The advective part is
274 solved using the explicit Discontinuous Finite Elements technique, which is specifically
275 designed to reduce numerical dispersion (Siegel et al., 1998). For its part, the diffusive term is
276 solved using Mixed Hybrid Finite Elements, a technique well known as being conservative
277 for diffusion problems, even at the scale of a single element (Younes et al., 2010). The time-
278 step strategies (initial time step, minimum/maximum time steps) are defined by the user and
279 automatically adapted by the code to read the flow data at the corresponding times, and also
280 to fulfill the Courant criterion. Consequently, global time steps are determined by the
281 following constraint:

282 $$\Delta t \le \min_{A} \left(\frac{2|A|}{\sum_{i=1}^{nb} \left| Q_{\Gamma_i}^{A} \right|} \right) \tag{15}$$

where *nb* is the number of faces (3-D) or edges (2-D), $|A|$ is the volume (3-D) or area (2-D) of the element A, $Q_{\Gamma_i}^{A}$ are water fluxes across each edge Γ_i. Fulfilling the Courant criterion avoids oscillations and contributes to the reduction of numerical diffusion. It is also worth noting that in all the simulated transport scenario the "element" longitudinal and transverse Peclet number have been kept to small values $\Delta x/\alpha_L \approx 1/5$, $\Delta x/\alpha_T \approx 1/0.5$ (Δx is the mean size of an element in the mesh). This features reduces the numerical dispersion (compared with actual dispersion) stemming from the eventual second-order truncation terms of the discrete advection term.

3. Model performance evaluation

3-1- Comparison strategy for models performance evaluation

To assess the accuracy of the established low-dimensional model for solute transport, simulations performed with the low-dimensional model NIHM-T (2-D flow plus transport) are compared to fully 3-D simulations of saturated/unsaturated flow and transport performed with TRACES 3-D. The comparisons are based on local concentration values (breakthrough curves - BTC) and spatial moments of the concentration plume. As concentrations provided by the 2-D simulations are mean values over the *z*-direction, a fair comparison with 3-D results suggests that concentrations provided by the 3-D simulations are also slightly processed to provide averages along *z*. These depth-averaged concentration values from the 3-D model are all weighted by the local fluxes for consistency with the 2-D transport model (see Eq. (10), which relies upon an averaged flux $\bar{\mathbf{q}}$). Assuming that the 3-D domain at a location (x, y) is discretized in N_L elements along the direction *z*, the depth averaged concentration $\bar{C}_E$ is given by:

306 $$\bar{C}_E = \sum_{j=1}^{N_L} C_j Q_j \Big/ \sum_{j=1}^{N_L} Q_j \quad (11)$$

307 where C_j [ML^{-3}] is the subsurface solute concentration in element *j* of the 3-D mesh, and Q_j

308 [ML^{-3}] is related water flux.

309 The zeroth- (total mass in the system), first- (center of mass), and second- (spread of

310 mass) order spatial moments of the concentration in the system inform the shape of the solute

311 plume. They are well suited to the comparison of different methods for solving transport (here

312 2-D versus 3-D) as they do not target local pinpoint accuracy of a transport simulation but

313 look at the overall behavior of the system. In many practical applications, local accuracy such

314 as precise evaluation of concentration values cannot be compared with actual test cases,

315 simply because the measurements do not exist. The first- and second-order spatial moments

316 depend on the direction along which they are calculated. In the various test cases discussed

317 below, these moments are only calculated along the *x*-direction corresponding to the main

318 flow direction of all settings. Moments are computed according to the following expressions:

319 $$M^0 = \sum_{E=1}^{NM} C_E \theta_E A_E \quad (12)$$

320 $$M_x^1 = \frac{\sum_{E=1}^{NM} C_E \theta_E A_E x_{gE}}{M^0} \quad (13)$$

321 $$M_x^2 = \frac{\sum_{E=1}^{NM} C_E \theta_E A_E x_{gE}^2}{M^0} - \left(M_x^1\right)^2 \quad (14)$$

322 where M^0 [M] is the zeroth-order moment, M_x^1 [L] is the first-order moment in the *x*-

323 direction, and M_x^2 [L^2] is the second-order moment in the *x*-direction, *E* is the index of a 2-D

324 or 3-D element of the grid, θ_E [-] is the average water content in element *E*, x_{gE} [L] is the *x*-

325 coordinate of the center of *E*, A_E [L^3] is the area/volume of element *E*, and *NM* is the total

number of elements in the domain. It is worth noting that the concentrations C_E in the calculations of moments from 3-D simulations are not averaged along the *z*-direction. Comparing moments from 2-D versus 3-D approaches can show possible discrepancies associated with the distributions of concentrations (and velocities) along *z* in a 3-D configuration and not seen by the 2-D calculations.

3-2- Synthetic test cases and scenarios

It was shown that for flow, the reduction of the subsurface dimensionality rendered simplified velocity fields without resulting in noticeable errors both on heads in the subsurface and water fluxes collected at various scales of the system (from, e.g., exfiltration at a spring to the surface, flowrates at the outlet of the watershed, or leaks through a subsurface boundary condition; Pan et al., 2015; Jeannot et al., 2018, 2019). However, these dimensionally reduced velocity fields could result in biased estimates of solute concentrations. In 2-D, the solute spreading over diverse streamlines is not correctly mimicked by transport along the single streamline averaging the diverse lines (in 3-D) stacked along the direction (*z*) of the flow integration.

For this paper, six scenarios were specifically designed to assess the ability of NIHM-T to describe flow and transport processes. Scenarios S1 to S5 rely upon the domain configuration given in Fig. 1, that is purposely set up to simplify the various interpretations that will be given when comparing 3-D and 2-D integrated transport results. The computational domain is a 100 m × 20 m × 10 m parallelepiped representing a synthetic unconfined aquifer. The bottom and top elevations of the domain are set to 0 m and 10 m, respectively. For the comparison with TRACES 3-D model, the whole domain is meshed via 56,000 hexahedron elements of uniform size (1 m) over *x* and *y* directions. Along the vertical (*z*) direction, the mesh is refined in the first meter, close to the surface, to improve numerical

stability and provide accurate numerical solutions in the unsaturated infiltration area. As a consequence, the subsurface model is discretized into 28 horizontal layers of increasing thickness from 10 cm at the top to 50 cm at the bottom. Regarding the low-dimensional 2-D model, the grid composed of 4,000 triangular elements and 2,121 nodes is obtained by splitting in two the four-edge horizontal facets of the first layer of the 3-D mesh. For the BTCs comparisons, the "element" 2-D concentrations are the average of the two elements split from the 3-D grid (to match the 3-D horizontal grid), and the "element" 3-D concentrations are the depth averaged concentrations over the 28 layers.

Flow and transport scenarios S1 to S5 were carried out in a heterogeneous block of hydraulic conductivity. The log10 hydraulic conductivities obey a spherical covariance function with a mean of -3.5, a variance of 1.0 (conductivities expressed in $m.s^{-1}$), and a correlation length of 60 m and 15 m in the horizontal and vertical directions, respectively (Fig. 1). The field has been generated using a sequential Gaussian method described in GSLIB (Geostatistical Software Library, Deutsch and Journel, 1997). All the other flow and transport parameters are considered uniform over space. The porosity is set to $\phi = 0.15$ and the specific storage to $Ss = 5\times10^{-3}$ m^{-1}. The parameters for the Mualem–Van Genuchten equations are set to $\alpha = 1$ m^{-1} and $n = 2$. For the transport problem, the longitudinal dispersivity coefficient is assigned $\alpha_L = 5$ m, the horizontal and vertical (for 3-D) transverse dispersivity coefficients are taken as $\alpha_T = 0.5$ m, and the molecular diffusion coefficient in the porous material is equal to 10^{-9} $m^2.s^{-1}$. For the 2-D domain, the hydraulic conductivities are integrated over depth, taking care to consider the different layer thicknesses. For flow, Dirichlet boundary conditions are prescribed on two opposite faces (at $x = 0$ and $x = 100$ m), while the other lateral faces and the bottom of the domain are considered as null-flux Neumann boundaries. Dirichlet head values are adjusted according to the targeted hydrological situations (fully saturated and partially saturated) described below. Using the

above-mentioned properties, different initial and boundary conditions for the flow and transport problems were defined in scenarios S1 to S5 under transient flow conditions, as summarized in Table 1. For the first scenario (S1), the domain is fully saturated. The initial hydraulic head is set at 10 m, and constant hydraulic heads are set to 12 m and 10 m at the Dirichlet boundaries, in x = 0 m and x = 100 m, respectively (Fig. 2). For the second scenario (S2), the domain is partially saturated with an initial water table located 3 m below the soil surface. The Dirichlet boundaries in x = 0 m and x = 100 m are set to H1 = 8 m and H2 = 7 m, respectively, as shown in Fig. 3. A uniform rainfall of 2×10^{-7} m.s^{-1} is applied during the first 5 days at the surface of the domain. The third scenario (S3) is close to the second one, but the initial water table and Dirichlet boundary conditions are chosen to increase the unsaturated thickness and assess the effect of the hydrostatic pressure assumption for flow on the simulated transport. The initial hydraulic head is thus set to 5 m. The constant hydraulic head H1 = 6 m is imposed at x = 0 m and H2 = 5 m is prescribed at x = 100 m (see Fig. 3). For solute transport, in the three configurations S1, S2, and S3, the initial concentration is equal to 0 except in a vertical column crossing the whole aquifer thickness and rectangular horizontal section extending within x = 26-32 m and y = 8-13 m (Fig. 2 and Fig. 3). At this location, the solute is injected through a source term evenly distributed over the 10 m depth of the system. The injected mass is set to 6×10^{-3} kg.s^{-1} for a duration of 3 days. All boundaries are set to zero solute dispersion flux. As contaminants can also reach groundwater from inlets at the land surface, additional scenarios (S4 and S5), only valid for the 3-D problem, limit the contaminant injection to a surface area, also located within x = 26-32 m, y = 8-13 m, but only over a thickness of 10 cm from the top of the domain, as shown in Fig. 4. In 2-D, S4 and S5 come down to an injection over the whole thickness of the system as 2-D simulations do not distinguish the surface from the depth. The flow problem in scenarios S4 and S5 is very similar to that of scenario S2, but for S4, to diminish the thickness of the unsaturated zone, the

401 initial hydraulic head is set to 9 m and constant hydraulic heads H1 = 10 m and H2 = 9 m are
402 imposed at x = 0 m and at x = 100 m, respectively (see Fig. 4). The simulated period is 16
403 days, and a maximum time step length of 1 hr is prescribed for both the flow and transport
404 simulations.

405 Scenario 6 (S6) is designed to assess the quality of the modeling approach in a more
406 complex configuration with a tilted and bumpy bottom of the aquifer, and more variable
407 hydrological conditions. The domain consists of two triangular hillslopes connected to a 140
408 m long and 6 m wide channel, presented in Fig. 5. The surface slopes in the x and y direction
409 are of 0.05 and 0.02, respectively. The substratum (bottom) elevation of the aquifer is first
410 defined by supposing it parallel to the surface with a thickness of the subsurface domain set to
411 20 m. Then, the elevation of the substratum for each computation node is modified to render a
412 bumped surface adding a perturbation randomly sampled with a +/- 1 m uniform distribution.

413 For the TRACES 3-D model, the whole system is meshed using 123,368 hexahedron
414 elements of uniform size (2 m) over x and y directions. The domain is discretized into 45
415 layers of increasing thickness along the vertical (z) direction. The computational mesh is
416 refined close to the surface to better capture the infiltration dynamics. For sake of consistency,
417 the integration in the flow model is performed using similar integration steps to evaluate the
418 equivalent 2-D parameters. The mesh grid in NIHM-T is composed of 3,220 triangular
419 elements generated as for the preceding applications by splitting in two the horizontal 2-D
420 elements of the top layer of the 3-D mesh.

421 The saturated hydraulic conductivity field is generated using the same technique as the
422 one for the previous scenarios, with an anisotropic spherical covariance of 60 m correlation
423 length in the horizontal directions and of 15 m in the vertical direction. The resulting
424 statistical distribution of the log10 of conductivity values is Gaussian, of mean -4.56 and
425 spans the range [-6.25, -2.95]. The heterogeneous conductivity field was first generated into a

426 parallelepiped – as shown in Fig. 6. – and then interpolated onto the computational meshes
427 used for both NIHM-T and TRACES. The Van Genuchten parameters α and n in the
428 relationships between saturation, water content and hydraulic conductivity are set to 1 m^{-1} and
429 2, respectively.

430 The lateral boundaries of the domain are considered as no-flow boundaries. Hydraulic
431 heads of 19 m and 24.8 m are imposed to the downhill and top limits of the domain,
432 respectively. The initial conditions are set using a linear interpolation between the boundary
433 conditions at the down and top limits. The total time of simulation is 800 days. Rainfall is
434 applied at the surface of the domain with a 2×10^{-7} $m.s^{-1}$ rate for 20 days every 60 days, thus
435 resulting in transient flow conditions over the whole simulation period. For transport, a source
436 term of 1.6×10^{-4} $kg.s^{-1}$ is imposed in the computational meshes located at the surface and
437 presented in orange in Fig. 5, for a duration of 300 days. In the transport problem, the
438 longitudinal dispersivity coefficient is assigned α_L = 5 m, the horizontal and vertical (for 3-D)
439 transverse dispersivity coefficients are taken as α_T = 0.5 m, and the molecular diffusion
440 coefficient in the porous material is equal to 10^{-9} $m^2.s^{-1}$. The evolutions over time of average
441 concentrations and statistical moments are compared between NIHM-T and TRACES -3D at
442 points #3 and #4, posted in Fig.5.
443
444 **4. Results and discussion**
445
446 Fig. 7 shows the evolution over time of the average concentrations in scenario S1 at
447 two selected points P1 (x = 50 m, y = 10 m) and P2 (x = 70 m, y = 13 m) displayed in Fig. 2.
448 The evolution of the first-order and second-order moments for the first scenario S1 are shown
449 in Fig. 8**.** The results produced by the low-dimensional approach and TRACES 3-D are very
450 close, with a maximum root mean square error (RMSE) for average concentrations of only

451 5.56×10^{-3} kg.m^{-3}. The BTCs and the evolution of the zeroth-, first- and second-order moments
452 demonstrate that in fully-saturated conditions, the low-dimensional model can accurately
453 reproduce the spatial evolution of the plume and the transport processes in a heterogeneous
454 saturated hydraulic conductivity field. This feature was expected in the absence of an
455 unsaturated zone, a specific case in which the averaging (integration) technique is reliable for
456 both flow and transport in heterogeneous porous media.

457 The pairs (Fig. 9, Fig. 10) and (Fig. 11, Fig. 12) display the evolutions of the same
458 variables, that is, BTCs in P1 and P2, and spatial moments for scenarios S2 and S3,
459 respectively. In both cases, the shapes of the BTCs are similar but with a maximum value of
460 concentrations higher for the 2-D approach and a maximum RMSE of 8.21×10^{-2} kg.m^{-3} for
461 average concentrations when the thickness of the unsaturated zone is the highest (S3, Fig. 11).
462 The zeroth-order moments show that the solute plumes reach the downstream boundary after
463 3 days (just when the solute injection has stopped), irrespective of the simulation S2 or S3 and
464 the 2-D versus 3-D approaches. The first-order moments are close at the beginning of the
465 simulation and become higher for the 2-D model. This observation goes with the fact that the
466 3-D simulation with an explicit representation of the vadose zone, might trap solute mass in
467 low velocity areas of the shallow subsurface. The mean location of the solute plume in 2-D
468 moves slightly quicker and also goes slightly farther downstream than in 3-D. In relation with
469 the eventual trapping of solute in the vadose zone of the 3-D model, the second-order
470 moments, associated with the spreading of concentration over space, are slightly higher for
471 the full model.

472 These differences between models increase with the thickness of the unsaturated zone
473 (compare Fig. 9 with Fig. 11, and Fig. 10 with Fig. 12) and could be the consequence of the
474 simplifications in the 2-D model, where the unsaturated zone is described by hydrostatic
475 heads only. The mean velocities along the z direction could not fully coincide with the mean

476 sampled by the 3-D model. The recharge in S2 and S3 also generates vertical velocities,
477 which cannot be properly taken into account in the integrated model, as we already mentioned
478 by stating that infiltration is only seen in NIHM as a variation of hydraulic heads. This is
479 confirmed by the snapshots presented in Fig. 13 and Fig. 14. For very similar shapes of the 2-
480 D solute plume between scenarios S2 and S3, the vertical cross sections of the 3-D model
481 clearly indicate that a thicker vadose zone increases the solute mass trapped just beneath the
482 surface. As told earlier**,** in the fully 3-D simulations, solute remains trapped in the unsaturated
483 zone where velocities are very low compared to the saturated zone. This trapping decreases
484 the concentration peaks, reduces the average velocity sampled by the solute, and increases the
485 dispersion of the contaminant in the 3-D configurations.

486 When the solute is only injected at the top surface of the domain, the reduced model
487 can underestimate the contaminant storage in the unsaturated zone. For the fourth scenario
488 (S4), where the vadose zone is thin (approximately one meter over the whole system), the
489 results in Fig. 15 and Fig. 16 clearly indicate that the low-dimensional model reproduces
490 fairly well the 3-D model results, with a maximum RMSE of 5.51 10^{-2}kg.m^{-3} for average
491 concentrations (Fig. 15). When the unsaturated zone is thicker (S5), its effects on solute
492 transport are amplified compared to those seen for the column-type concentration source. The
493 solute which was initially only concentrated in the upper part of the unsaturated zone, remains
494 trapped in areas of weak velocities. Only a little mass experiences the higher velocities of the
495 saturated zone beneath. Therefore, the overall transport is retarded, renders lower solute peak
496 values (Fig. 17 and 18) and increased spreading (Fig. 18). This is confirmed by the evolution
497 of the zeroth-order moments, which illustrate a faster reduction in contaminant mass from day
498 three in the reduced model.

499 The results presented in Fig. 19 and Fig. 20. for scenario S6 (whose geometrical and
500 hydrological conditions are more complex) show the same overall trend for both average

concentration and statistical moments evolutions. As the unsaturated zone is deeper at point #3 than at point #4 (due to the initial conditions) the difference between the average concentrations produced by NIHM-T and TRACES 3-D is more pronounced at point #3. At both locations, the reduced model performs well and is able to capture the transport dynamics. The evolution over time of the zeroth-, first-, and second-order moments plot in Fig. 20 also show that NIHM-T captures the spatial evolution of the plume, even if the geometrical configuration of the domain and the history of flow and transport are more complex.

Regarding the computational cost, CPU times are recorded and compared for each model. Both models NIHM-T and TRACES 3-D are calculated on a standard desktop computer and the calculation time is related to the simulation period (Scenarios S1 to S5: 16 days; Scenario S6: 800 days). The gain in computation time using the integrated model NIHM is notable when reproducing subsurface flow and solute transport. Table 2 lists CPU times by distinguishing them between solving flow or transport. As expected, the low-dimensional approach significantly reduces CPU times. This is linked to the number of unknowns (Scenarios S1 to S5: 12,240 in 2-D, and 346,720 in 3-D; Scenario S6: 9,886 in 2-D, and 768,912 in 3-D) and non-linear flow conditions in the unsaturated zone. We recall here that flow in the unsaturated zone is solved explicitly in 3-D and described by hydrostatic conditions in the low-dimensional model.

5. Conclusions

A low-dimensional model has been proposed to describe the non-reactive transport behavior of contaminants in the subsurface. This investigation shows that the advection-dispersion equation can be expressed with a reduced dimensionality by relying upon the low-dimensional hydrological model NIHM which calculates averaged water fluxes considering both the unsaturated and saturated zones of a shallow subsurface system. The proposed

526 approach has been tested on different heterogeneous synthetic test cases via a comparison
527 with a full 3-D approach for both flow and transport.

528 The results indicate that the reduced model NIHM-T for both coupled flow and
529 transport performs well under saturated-flow conditions, even in heterogeneous systems.
530 When applied to partially saturated heterogeneous aquifers, the presence of a vadose zone can
531 add further complexity because of the non-negligible three-directional components of water
532 fluxes and their variations over time and space in the subsurface. As the low-dimensional
533 model neglects the vertical components of flow, assuming hydrostatic conditions, the
534 resulting mean water velocity fields can be partially flawed. The main impact on transport
535 comes from the relative thickness of the unsaturated zone compared with that of the saturated
536 zone. In the 2-D approach (with flow integrated normal to bedrock), the hydrostatic
537 assumption needed for building an averaged 2-D field of mean velocities may overlook the
538 variability of hydraulic conductivities due to variable saturations.

539 The direct result is a raw evaluation of water velocities in the system which directly
540 impacts solute transport. The 3-D configurations with sources of concentrations uniformly
541 distributed over the whole thickness of the system can be correctly reproduced by a 2-D
542 calculation, simply because an injection at the surface in 2-D is equivalent to a uniform
543 injection over depth in 3-D. For the 3-D problems where the injection plug is limited to the
544 first top layers of the domain, the 3-D calculations will account for variable injection
545 conditions over depth according to infiltration and vertical flow components.

546 For its part, the 2-D approach will still consider that the concentration at the injection
547 plug is uniform over depth. In such applications, the results reveal that the approximations
548 associated with the integration of flow in 2-D (NIHM) increase discrepancies between 2-D
549 and 3-D as the thickness of the unsaturated zone increases, and infiltration and time-varying
550 vertical water velocities become key features of the hydrological system.

However, and notwithstanding its basic assumptions, the reduced model is found to be practical for simulating solute transport in porous media for shallow aquifers. In addition to simplifying mass transfer modeling, it is worth mentioning that the CPU time required for the reduced model is significantly less compared to a full 3-D calculation. Overall, in this study, the low-dimensional model is highlighted as an alternative for simulating water quality. With this aim in mind, further works would couple surface and subsurface solute transport processes to investigate actual complex watersheds and their questions relative to water quality challenges.

Acknowledgments

The financial support of the GIS 'Institut de Mathématiques pour la Planète Terre' is acknowledged.

References

Barry, D.A., 1992. Modelling contaminant transport in the subsurface: Theory and computer programs. H. Ghadiri, C.W. Rose (Eds.), Modelling Chemical Transport in Soil: Natural and Applied Contaminants, Lewis Publishers, Boca Raton.

Barry, D.A., Parker, J.C., 1987. Approximations for solute transport through porous media with flow transverse to layering. Transp. Porous Med. 2. https://doi.org/10.1007/BF00208537

Bear, J., 1972. Dynamics of Fluids in Porous Media. American Elsevier Publishing Company, New York, 764 p.

Bosma, W.J.P., van der Zee, S.E.A.T.M., 1992. Analytical approximations for nonlinear adsorbing solute transport in layered soils. J. Contam. Hydrol. 10, 99–118. https://doi.org/10.1016/0169-7722(92)90025-A

Boso, F., Bellin, A., Dumbser, M., 2013. Numerical simulations of solute transport in highly heterogeneous formations: A comparison of alternative numerical schemes. Adv. Water Resour. 52, 178–189. https://doi.org/10.1016/j.advwatres.2012.08.006

Burri, N.M., Weatherl, R., Moeck, C., Schirmer, M., 2019. A review of threats to groundwater quality in the anthropocene. Sci. Total Environ. 684, 136–154. https://doi.org/10.1016/j.scitotenv.2019.05.236

Carnahan, B., Lutter, H.A., Wilkes, J.O., 1969. Applied Numerical Methods. Wiley, New York.

Chapman, S.W., Parker, B.L., 2005. Plume persistence due to aquitard back diffusion following dense nonaqueous phase liquid source removal or isolation: plume persistence due to back diffusion. Water Resour. Res. 41. https://doi.org/10.1029/2005WR004224

Charbel Pierre El Soueidy, Anis Younès, Philippe Ackerer. Solving the advection-diffusion equation on unstructured meshes with discontinuous/mixed finite elements and a local time stepping procedure. International Journal for Numerical Methods in Engineering, Wiley, 2009, 79 (9), pp.1068-1093. https://doi.org/10.1002/nme.2609

Colombo, L., Alberti, L., Mazzon, P., Formentin, G., 2019. Transient flow and transport modelling of an historical CHC Source in North-West Milano. Water 11, 1745. https://doi.org/10.3390/w11091745

Craig, J.R., Rabideau, A.J., 2006. Finite difference modeling of contaminant transport using analytic element flow solutions. Adv. Water Resour. 29, 1075–1087. https://doi.org/10.1016/j.advwatres.2005.08.010

Crouzeix, M., Raviart, P.A., 1973. Conforming and nonconforming finite element methods for solving the stationary Stokes equations I. R.A.I.R.O. 7, R3, 33–76. https://doi.org/10.1051/m2an/197307R300331

Delay, F., Ackerer, P., 2016. The reduction of hydrological models for less tedious practical applications. C-R. Geoscience 348, 89–98. https://doi.org/10.1016/j.crte.2015.08.002

603 Deutsch, C.V., Journel, A.G., 1997. GSLIB Geostatistical Software Library and User's Guide,
604 Second Edition. ed. Oxford University Press, New York.

605 Dou, C., Woldt, W., Bogardi, I., Dahab, M., 1997. Numerical solute transport simulation
606 using fuzzy sets approach. J. Contam. Hydrol. 27, 107–126.
607 https://doi.org/10.1016/S0169-7722(96)00047-2

608 Graf, T., Therrien, R., 2005. Variable-density groundwater flow and solute transport in porous
609 media containing non-uniform discrete fractures. Adv. Water Resour. 28, 1351–1367.
610 https://doi.org/10.1016/j.advwatres.2005.04.011

611 Harbaugh, A.W., Banta, E.R., Hill, M.C., McDonald, M.G., 2000. MODFLOW-2000, The
612 U.S. Geological Survey Modular Ground-Water Model - User guide to modularization
613 concepts and the ground-water flow process (No. Open-file report 00-92), Open-File
614 Report. U.S. Geological Survey: Reston, VA, USA.

615 Jeannot, B., Weill, S., Eschbach, D., Schmitt, L., Delay, F., 2019. Assessing the effect of
616 flood restoration on surface–subsurface interactions in Rohrschollen Island (Upper Rhine
617 river – France) using integrated hydrological modeling and thermal infrared imaging.
618 Hydrol. Earth Syst. Sci. 23, 239–254. https://doi.org/10.5194/hess-23-239-2019

619 Jeannot, B., Weill, S., Eschbach, D., Schmitt, L., Delay, F., 2018. A low-dimensional
620 integrated subsurface hydrological model coupled with 2-D overland flow: Application
621 to a restored fluvial hydrosystem (Upper Rhine River – France). J. Hydrol. 563, 495–
622 509. https://doi.org/10.1016/j.jhydrol.2018.06.028

623 Kong, J., Shen, C., Luo, Z., Hua, G., Zhao, H., 2016. Improvement of the hillslope-storage
624 Boussinesq model by considering lateral flow in the unsaturated zone: Influence of
625 unsaturated lateral flow on hillslope drainage. Water Resour. Res. 52, 2965–2984.
626 https://doi.org/10.1002/2015WR018054

627 Konikow, L.F., Sanford, W.E., Campbell, P.J., 1997. Constant-concentration boundary
628 condition: Lessons from the Hydrocoin variable-density groundwater benchmark
629 problem. Water Resour. Res. 33, 2253–2261. https://doi.org/10.1029/97WR01926

630 Leij, F.J., Van Genuchten, M.Th., 1995. Approximate analytical solutions for solute transport
631 in two-layer porous media. Transp. Porous Med. 18, 65–85.
632 https://doi.org/10.1007/BF00620660

633 Lyra, A., Loukas, A., Sidiropoulos, P., 2021. Impacts of irrigation and nitrate fertilization
634 scenarios on groundwater resources quantity and quality of the Almyros Basin, Greece.
635 Water Suppl. ws2021097. https://doi.org/10.2166/ws.2021.097

636 McDonald, M.G., Harbaugh, A.W., 1988. A modular three-dimensional finite-difference
637 ground-water flow model. https://doi.org/10.3133/twri06A1

638 Moeck, C., Radny, D., Auckenthaler, A., Berg, M., Hollender, J., Schirmer, M., 2017.
639 Estimating the spatial distribution of artificial groundwater recharge using multiple
640 tracers. Isot. Environ. Health S. 53, 484–499.
641 https://doi.org/10.1080/10256016.2017.1334651

Pan, Y., Weill, S., Ackerer, P., Delay, F., 2015. A coupled stream flow and depth-integrated subsurface flow model for catchment hydrology. J. Hydrol. 530, 66–78. https://doi.org/10.1016/j.jhydrol.2015.09.044

Richards, L.A., 1931. Capillary conduction through porous mediums. J. Appl. Phys. 1, 318–333. https://dx.doi.org/10.1063/1.1745010

Rizzo, C.B., de Barros, F.P.J., Perotto, S., Oldani, L., Guadagnini, A., 2018. Adaptive POD model reduction for solute transport in heterogeneous porous media. Comput. Geosci. 22, 297–308. https://doi.org/10.1007/s10596-017-9693-5

Robinson, B.A., Lu, Z., Pasqualini, D., 2012. Simulating solute transport in porous media using model reduction techniques. Applied Mathematics 03, 1161–1169. https://doi.org/10.4236/am.2012.310170

Rocha, D., Feyen, J., Dassargues, A., 2007. Comparative analysis between analytical approximations and numerical solutions describing recession flow in unconfined hillslope aquifers. Hydrogeol. J. 15, 1077–1091. https://doi.org/10.1007/s10040-007-0170-4

Selim, H.M., 1992. Modeling the transport and retention of inorganics in soils, in: Adv. Agron.. Elsevier, pp. 331–384. https://doi.org/10.1016/S0065-2113(08)60493-9

Siegel, P., Mosé, R., Ackerer, Ph., Jaffre, J., 1998. Solution of the advection-diffusion equation using a combination of discontinuous and mixed finite elements. International Journal for Numerical Methods in Fluids 24, 6, 595-613.

Shan, C., Javandel, I., 1997. Analytical solutions for solute transport in a vertical aquifer section. J. Contam. Hydrol. 27, 63–82. https://doi.org/10.1016/S0169-7722(96)00045-9

Sirovich, L., 1987. Turbulence and the dynamics of coherent structures. II. Symmetries and transformations. Quart. Appl. Math. 45, 573–582. https://doi.org/10.1090/qam/910463

Tartakovsky, D.M., 2000. An analytical solution for two-dimensional contaminant transport during groundwater extraction. J. Contam. Hydrol. 42, 273–283. https://doi.org/10.1016/S0169-7722(99)00086-8

Therrien, R., Sudicky, E.A., 1996. Three-dimensional analysis of variably-saturated flow and solute transport in discretely-fractured porous media. J. Contam. Hydrol. 23, 1–44. https://doi.org/10.1016/0169-7722(95)00088-7

Troch, P.A., Paniconi, C., Emiel van Loon, E., 2003. Hillslope-storage Boussinesq model for subsurface flow and variable source areas along complex hillslopes: 1. Formulation and characteristic response: Hillslope-storage Boussinesq model, 1. Water Resour. Res. 39. https://doi.org/10.1029/2002WR001728

van Genuchten, M.Th., 1980. A closed-form equation for predicting the hydraulic conductivity of unsaturated soils. Soil Sci. Soc. Am. Journal 44, 892–898. https://doi.org/10.2136/sssaj1980.03615995004400050002x

Wakida, F.T., Lerner, D.N., 2005. Non-agricultural sources of groundwater nitrate: a review and case study. Water Res. 39, 3–16. https://doi.org/10.1016/j.watres.2004.07.026

Weill, S., Delay, F., Pan, Y., Ackerer, P., 2017. A low-dimensional subsurface model for saturated and unsaturated flow processes: ability to address heterogeneity. Comput. Geosci. 21, 301–314. https://doi.org/10.1007/s10596-017-9613-8

Wu, S., Jeng, D., 2017. Numerical modeling of solute transport in deformable unsaturated layered soil. Water Sci. Eng. 10, 184–196. https://doi.org/10.1016/j.wse.2017.09.001

Younes, A., P. Ackerer, Delay, F., 2010. Mixed finite elements for solving 2-D diffusion-type equations, Rev. Geophys. 48, RG1004, https://doi:10.1029/2008RG000277.

Zheng, C., Bennett, G.D., 2002. Applied contaminant transport modeling, 2nd Edition. Wiley J. & Sons, Inc. ISBN: 978-0-471-38477-9, 656 p.

Zheng, C., Wang, P.P., 1999. MT3DMS: A modular three-dimensional multispecies transport model for simulation of advection, dispersion, and chemical reactions of contaminants in groundwater systems; Documentation and User's Guide.

Zheng, Y., Yu, C., Cheng, Y.-S., Lee, C., Simmons, C.W., Dooley, T.M., Zhang, R., Jenkins, B.M., VanderGheynst, J.S., 2012. Integrating sugar beet pulp storage, hydrolysis and fermentation for fuel ethanol production. Appl. Energ. 93, 168–175. https://doi.org/10.1016/j.apenergy.2011.12.084

Figure and table captions

Fig.1. Model geometry and the associated hydraulic conductivity field in the subsurface.

Fig.2. Horizontal cut view of boundary conditions for the saturated test case. Stars indicate locations used to compare breakthrough curves from transport simulation results.

Fig.3. Vertical cross section of the domain with top, bottom, and lateral (prescribed heads H1 and H2) boundary conditions for simulating unsaturated flow and solute transport– scenarios S2 and S3.

Fig.4. Vertical cross section of the domain with top, bottom, and lateral (prescribed heads H1 and H2) boundary conditions for simulating unsaturated flow and solute transport – scenarios S4 and S5.

Fig.5. Geometrical settings of the irregular domain.

Fig.6. Hydraulic conductivity field in the subsurface populating the irregular domain (black triangle as the trace at the surface of the domain).

Fig.7. Comparison of the evolutions over time of the average concentrations at the locations P1 and P2 - scenario S1.

Fig.8. Comparison of the evolutions over time of the zeroth-, first-, and second-order moments - scenario S1.

Fig.9. Comparison of the evolutions over time of the average concentrations at the locations P1 and P2 – scenario S2.

Fig.10. Comparison of the evolutions over time of the zeroth-, first-, and second-order moments - scenario S2.

Fig. 11. Comparison of the evolutions over time of the average concentrations at the locations P1 and P2 – scenario S3.

Fig.12. Comparison of the evolutions over time of the zeroth-, first-, and second-order moments - scenario S3.

Fig.13. (a)-Horizontal views of the 2-D solute plume simulated by the reduced model NIHM. (b)- Vertical cross sections through the 3-D solute plume simulated by the full model TRACES 3-D – scenario S2.

Fig.14. (a)-Horizontal views of the 2-D solute plume simulated by the reduced model NIHM. (b)- Vertical cross sections through the 3-D solute plume simulated by the full model TRACES 3-D – scenario S3.

Fig.15. Comparison of the evolutions over time of the average concentrations at the locations P1 and P2 – scenario S4.

Fig.14. Comparison of the evolutions over time of the zeroth-, first-, and second-order moments - scenario S4.

Fig.17. Comparison of the evolutions over time of the average concentrations at the locations P1 and P2 – scenario S5.

Fig.18. Comparison of the evolutions over time of the zeroth-, first-, and second-order moments - scenario S5.

Table.1. Flow and solute transport conditions for the 6 transport scenarios.

Table.2. Comparison of the values of CPU time in minutes recorded for the simulation of flow and solute transport for the 6 scenarios.

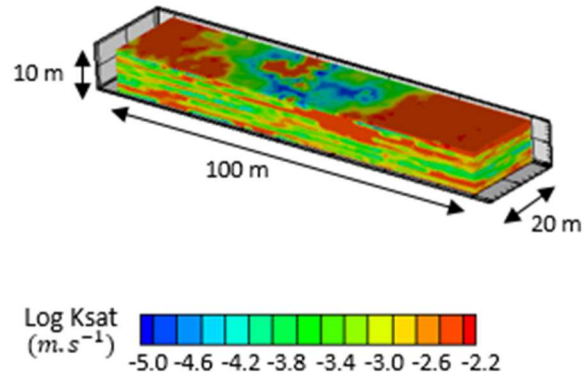

Fig.1. Model geometry and the associated hydraulic conductivity field in the subsurface.

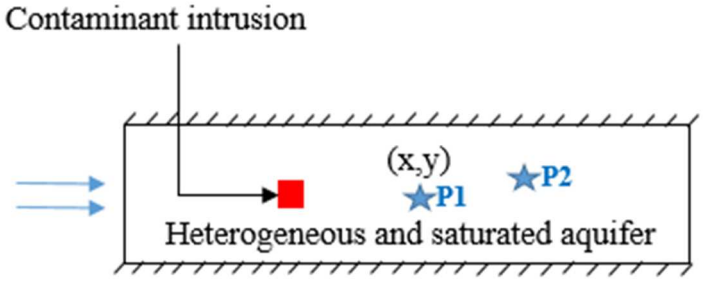

Fig.2. Horizontal cut view of boundary conditions for the saturated test case. Stars indicate locations used to compare breakthrough curves from transport simulation results.

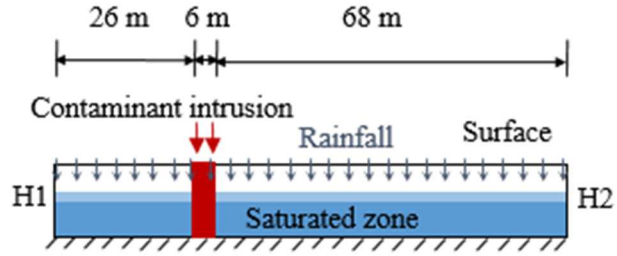

Fig.3. Vertical cross section of the domain with top, bottom, and lateral (prescribed heads H1 and H2) boundary conditions for simulating unsaturated flow and solute transport– scenarios S2 and S3.

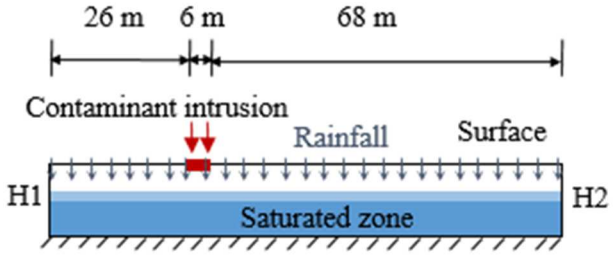

Fig.4. Vertical cross section of the domain with top, bottom, and lateral (prescribed heads H1 and H2) boundary conditions for simulating unsaturated flow and solute transport – scenarios S4 and S5.

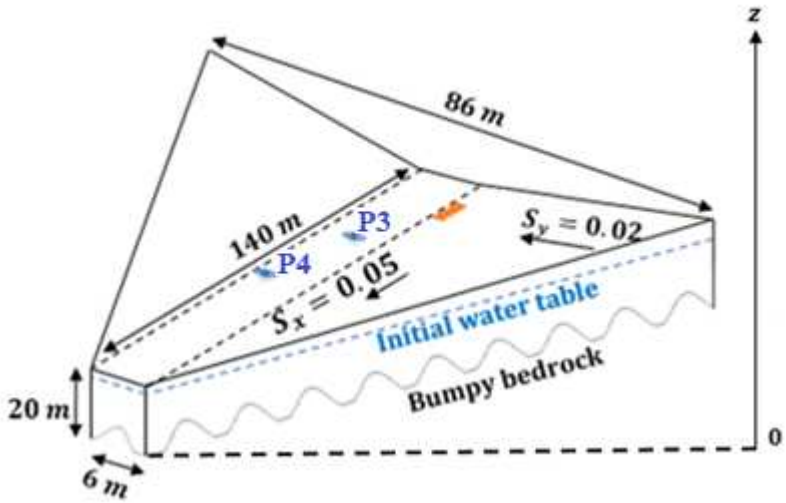

Fig.5. Geometrical settings of the irregular domain

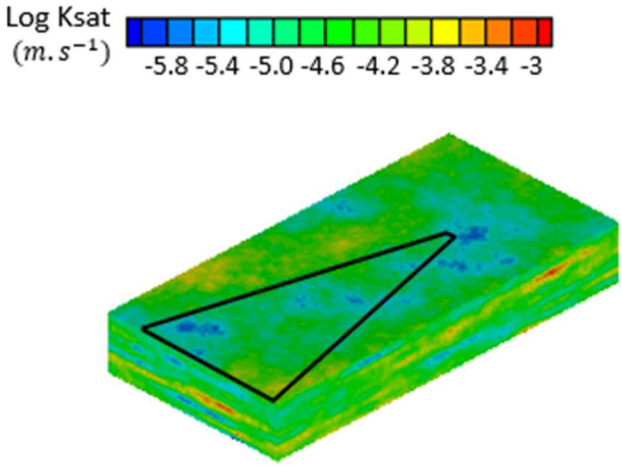

Fig.6. Hydraulic conductivity field in the subsurface populating the irregular domain (black triangle as the trace at the surface of the domain)

Table.1. Flow and solute transport conditions for the 6 scenarios.

Scenario	**S1**	**S2**	**S3**	**S4**	**S5**	**S6**
Sat: Saturated System **Unsat: Unsaturated System**	Sat	Unsat	Unsat	Unsat	Unsat	Unsat
Flow Model						
Initial hydraulic head (m)	10	7	5	9	7	19-24.8
Rainfall intensity ($m.s^{-1}$)	-	2×10^{-7}	2×10^{-7}	2×10^{-7}	2×10^{-7}	2×10^{-7}
Rainfall duration (d)	-	5	5	5	5	20 (×12)
Transport Model						
Initial concentration ($kg.m^{-3}$)	0	0	0	0	0	0
Injected mass ($kg.s^{-1}$)	6×10^{-3}	6×10^{-3}	6×10^{-3}	6×10^{-3}	6×10^{-3}	1.6×10^{-4}
Injection duration (d)	3	3	3	3	3	300
Injection zone thickness (m)	10	10	10	0.1	0.1	0.1

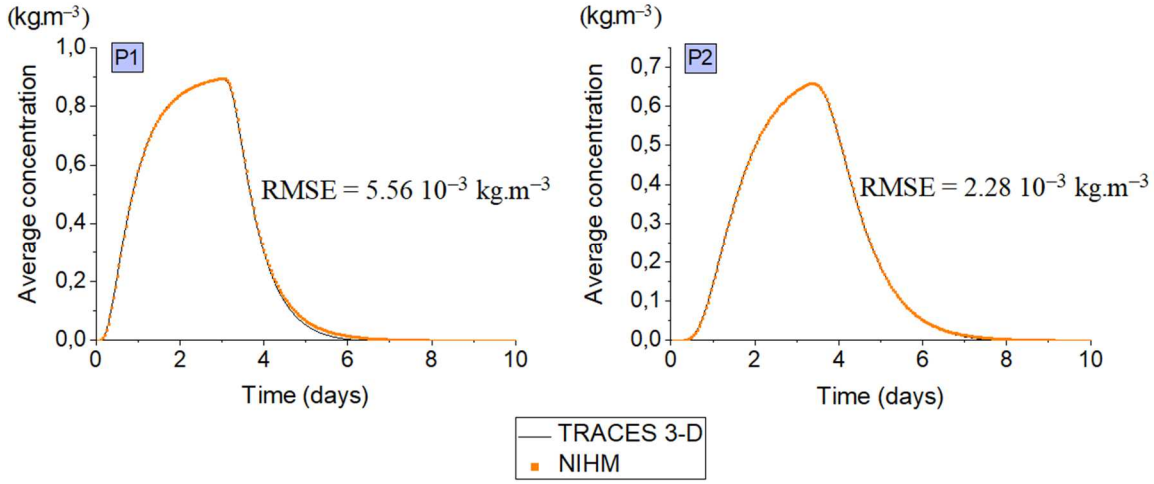

Fig.7. Comparison of the evolutions over time of the average concentrations at the locations P1 and P2 - scenario S1.

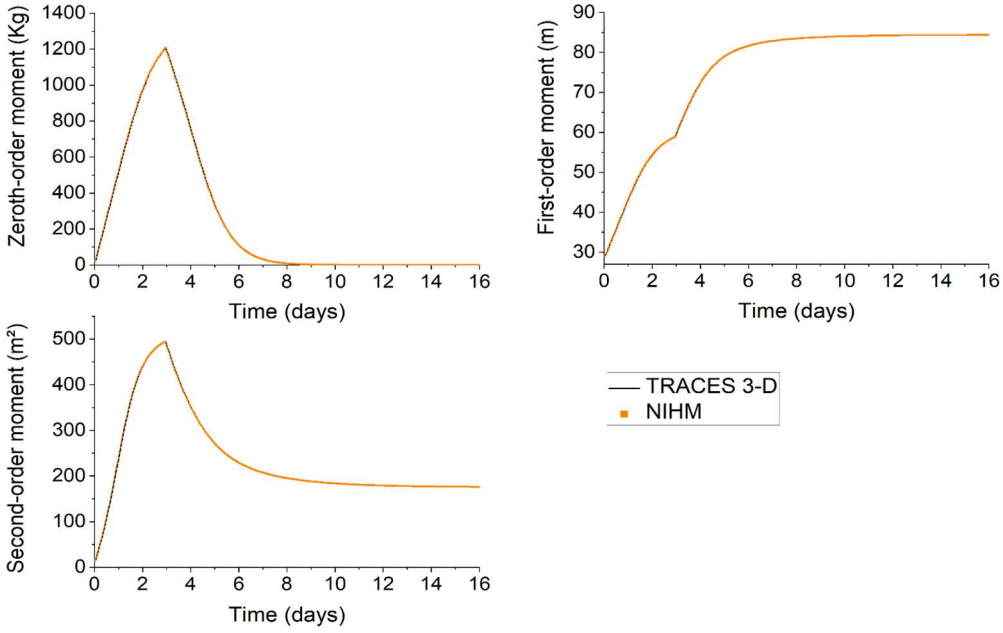

Fig.8. Comparison of the evolutions over time of the zeroth-, first-, and second-order moments - scenario S1.

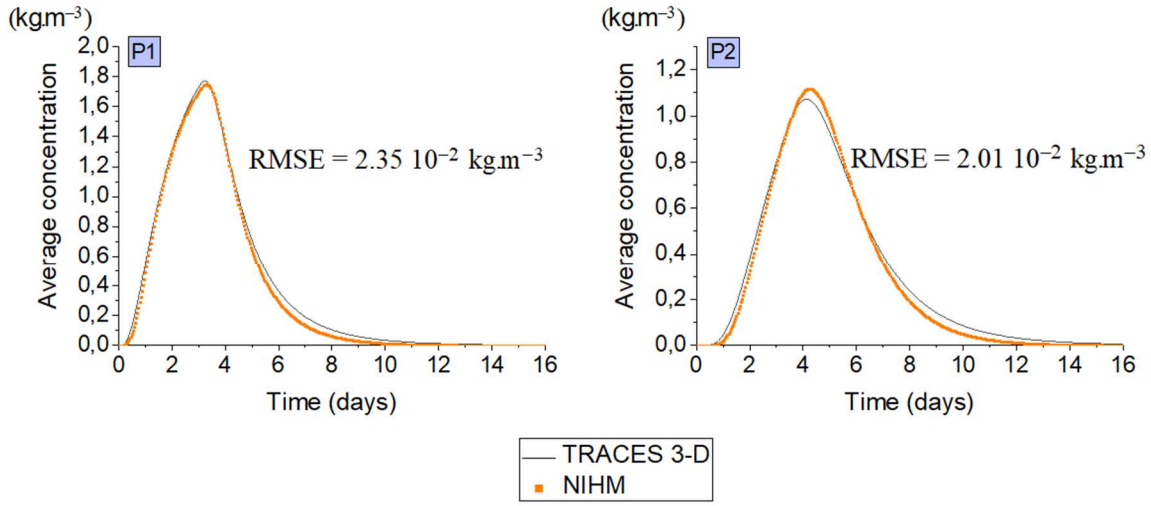

Fig.9. Comparison of the evolutions over time of the average concentrations at the locations P1 and P2 – scenario S2.

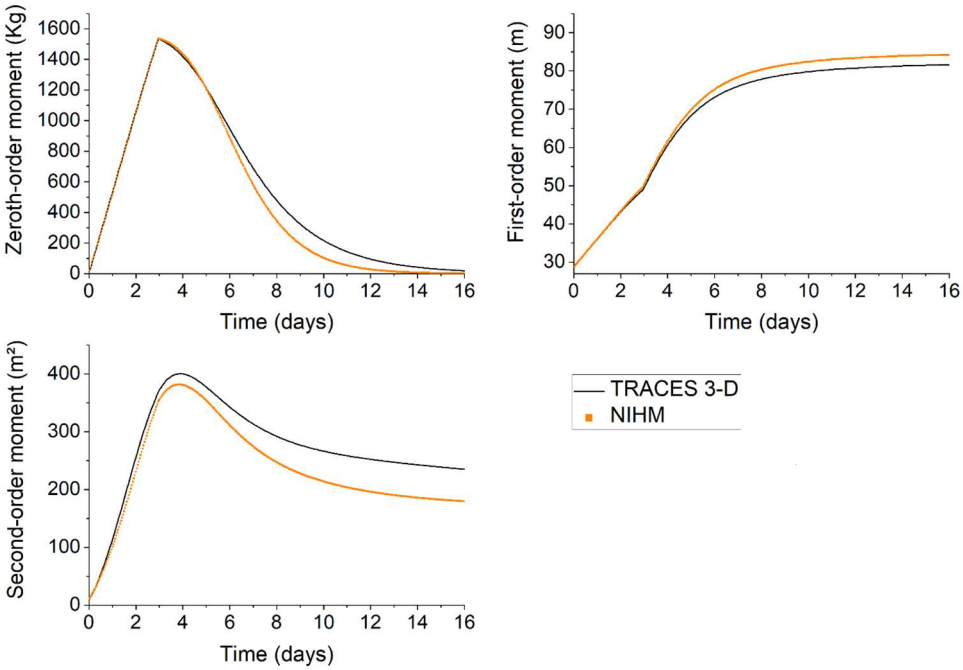

Fig.10. Comparison of the evolutions over time of the zeroth-, first-, and second-order moments - scenario S2.

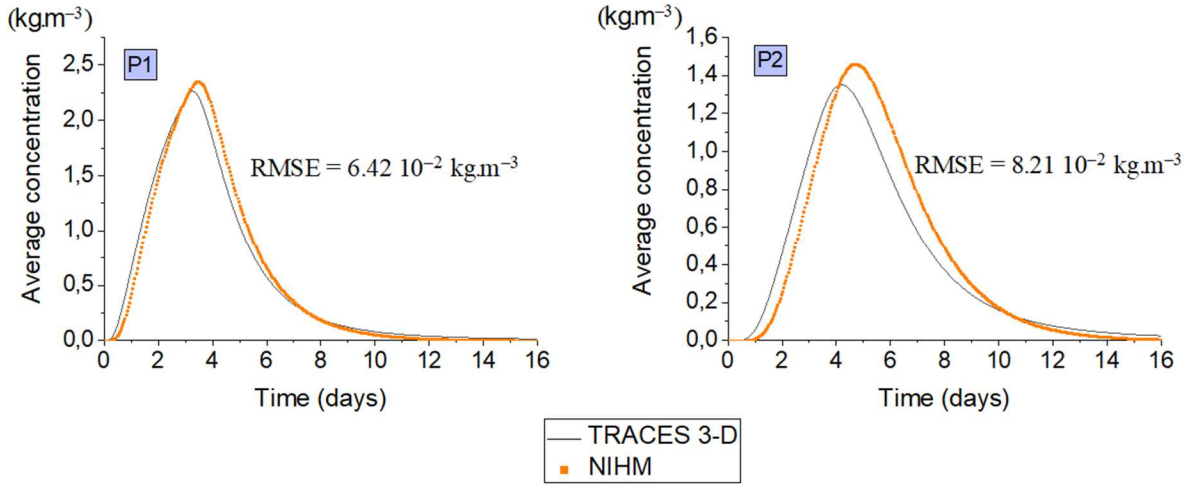

Fig.11. Comparison of the evolutions over time of the average concentrations at the locations P1 and P2 – scenario S3.

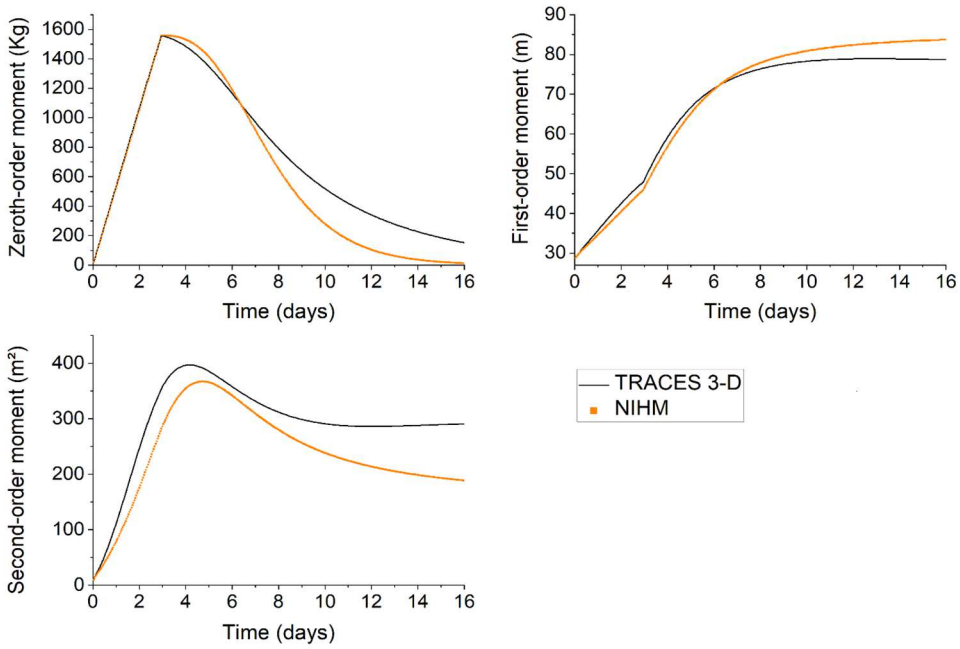

Fig.12. Comparison of the evolutions over time of the zeroth-, first-, and second-order moments - scenario S3.

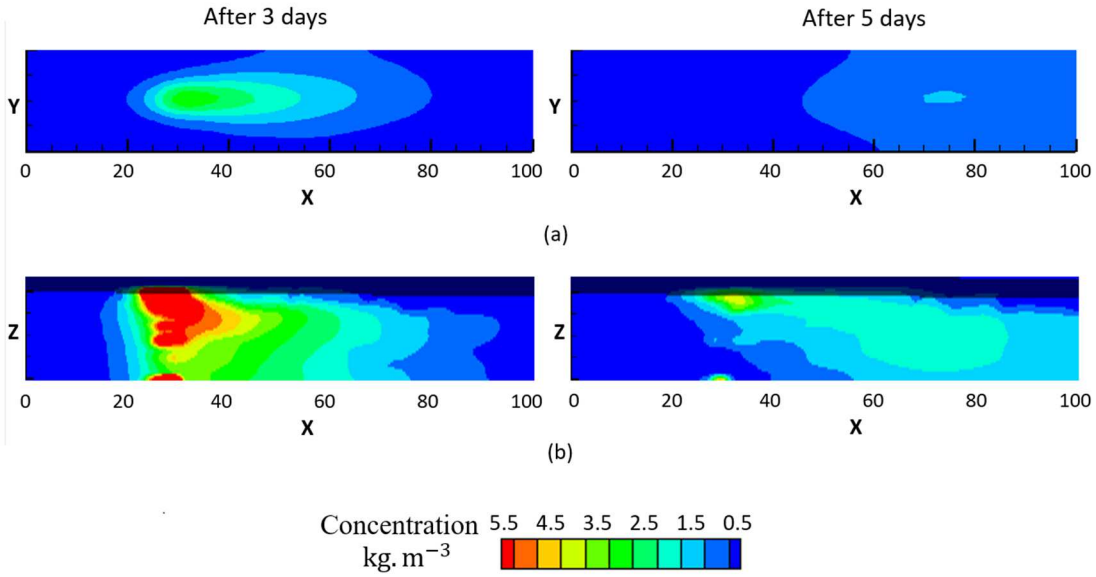

Fig.13. (a)-Horizontal views of the 2-D solute plume simulated by the reduced model NIHM. (b)- Vertical cross sections through the 3-D solute plume simulated by the full model TRACES 3-D – scenario S2.

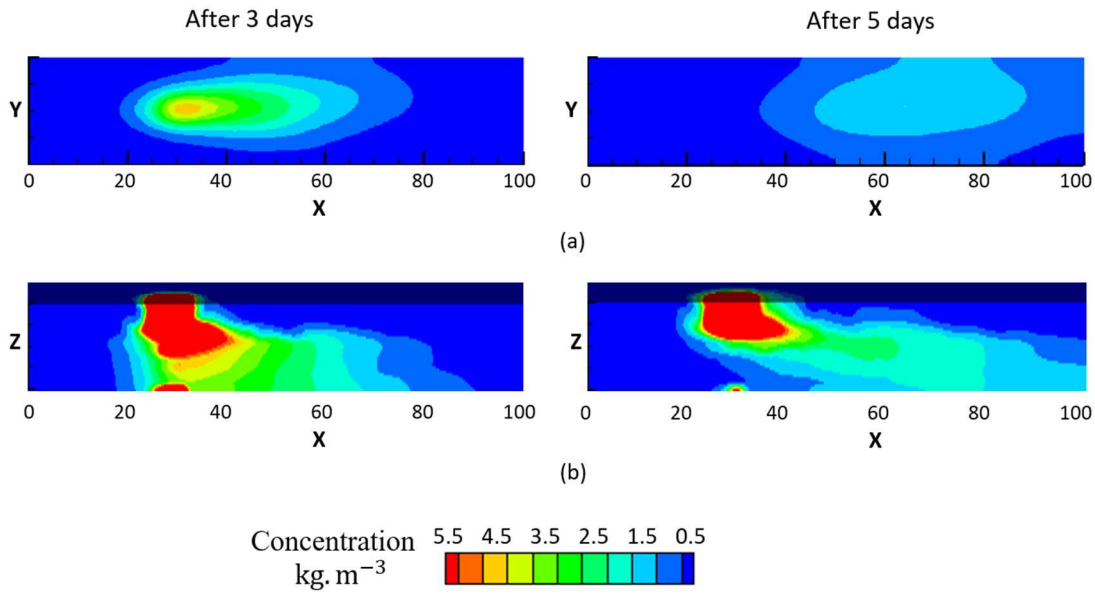

Fig.14. (a)-Horizontal views of the 2-D solute plume simulated by the reduced model NIHM. (b)- Vertical cross sections through the 3-D solute plume simulated by the full model TRACES 3-D – scenario S3.

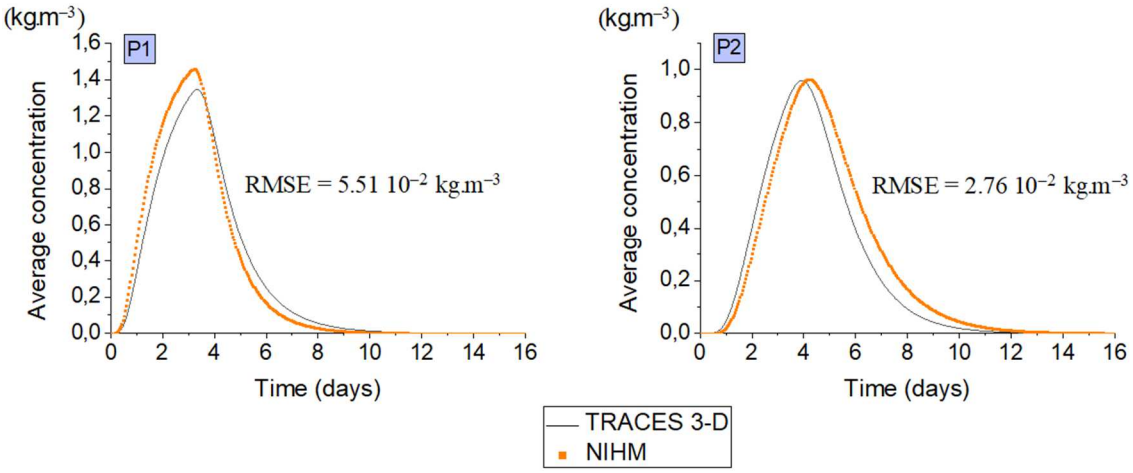

Fig.15. Comparison of the evolutions over time of the average concentrations at the locations P1 and P2 – scenario S4.

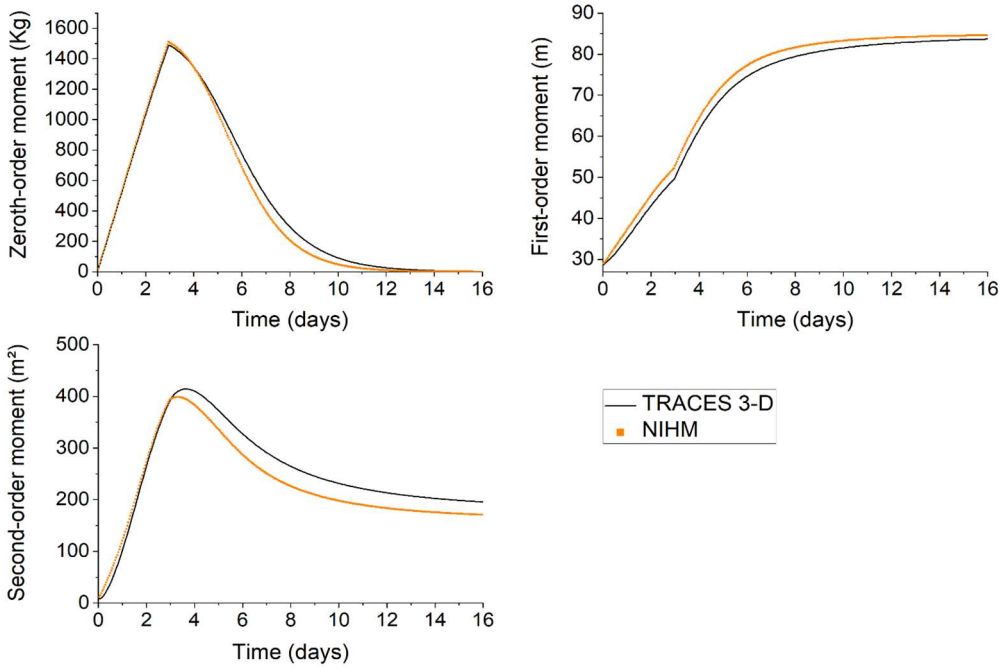

Fig.16. Comparison of the evolutions over time of the zeroth-, first-, and second-order moments - scenario S4.

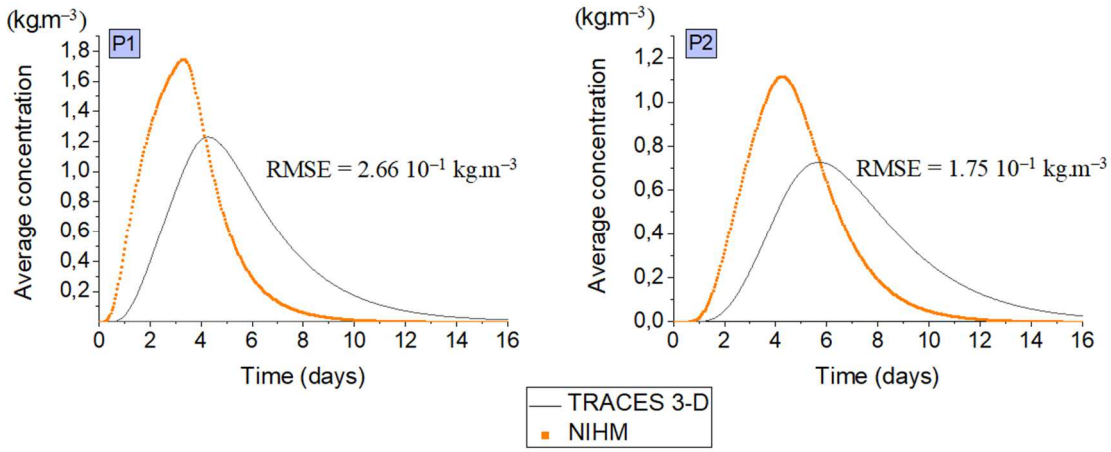

Fig.17. Comparison of the evolutions over time of the average concentrations at the locations P1 and P2 – scenario S5.

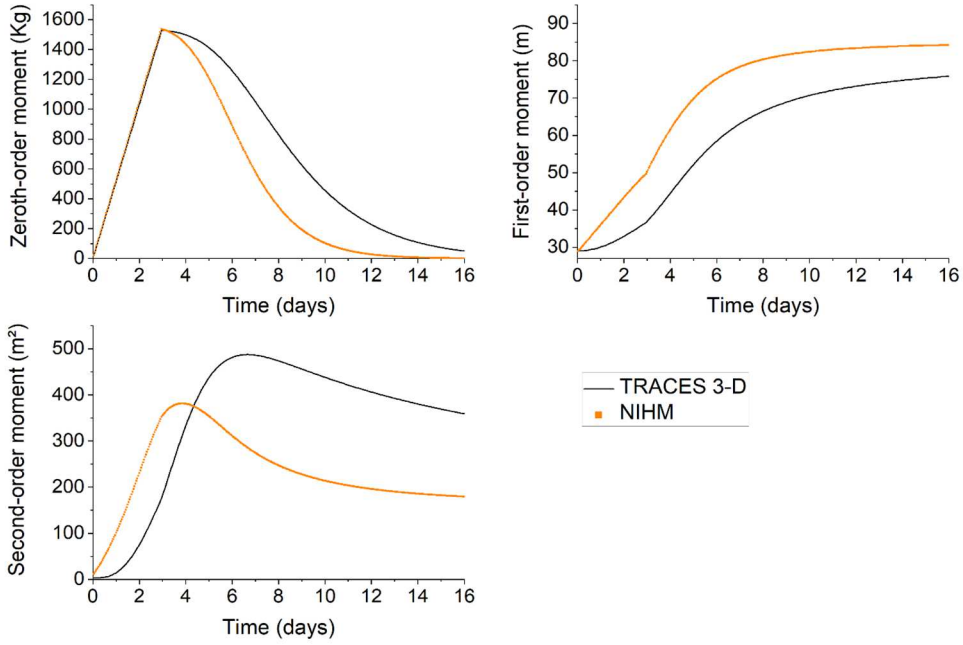

Fig.18. Comparison of the evolutions over time of the zeroth-, first-, and second-order moments - scenario S5.

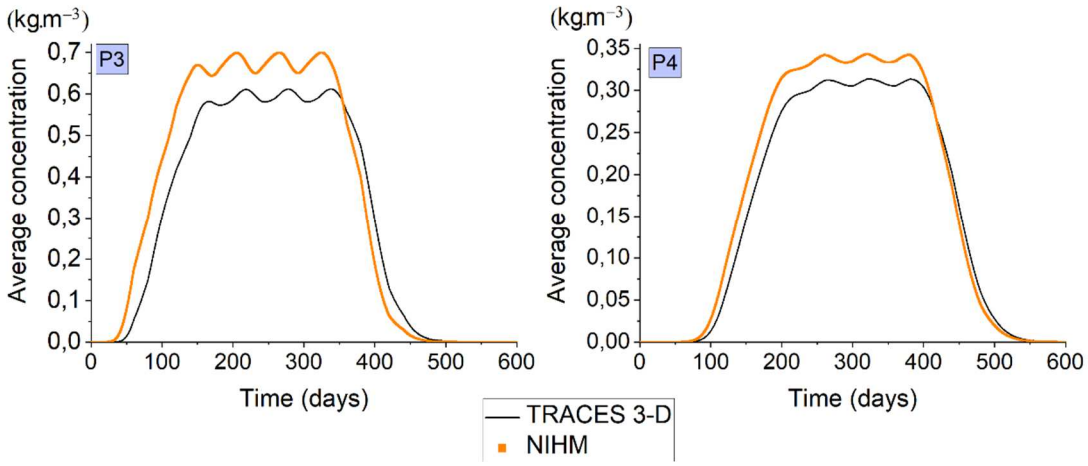

Fig.19. Comparison of the evolutions over time of the average concentrations at the locations P3 and P4 – scenario S6.

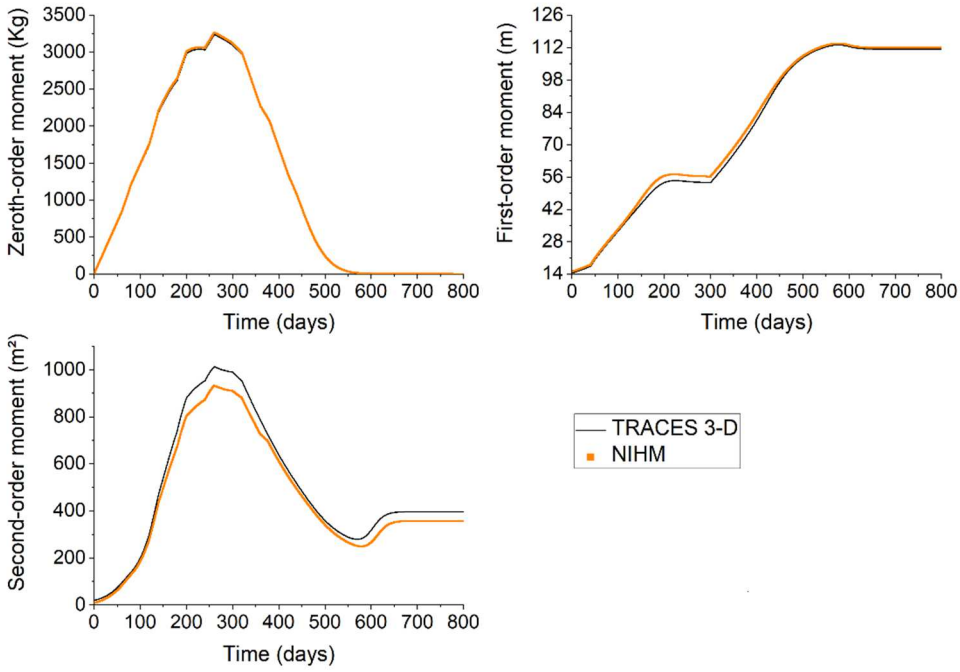

Fig.20. Comparison of the evolutions over time of the zeroth-, first-, and second-order moments - scenario S6.

Table.2. Comparison of the values of CPU time in minutes recorded for the simulation of flow and solute transport for the 6 scenarios.

	3-D flow	**3-D transport**	**3-D full model**	**2-D integrated flow**	**2-D integrated transport**	**2-D integrated full model**	**CPU ratio (3-D/2-D)**
S1	131.43	154.93	**286.36**	5.28	1.12	**6.40**	**44.74**
S2	98.22	171.96	**270.18**	6.92	1.06	**7.98**	**33.86**
S3	93.93	175.06	**268.99**	5.53	0.98	**6.51**	**41.32**
S4	104.75	178.76	**283.51**	4.97	0.94	**5.91**	**47.97**
S5	98.03	171.75	**269.78**	6.92	1.06	**7.98**	**33.81**
S6	5224.79	5405.98	**10630.77**	70.88	53.94	**124.82**	**85.17**